

Possible Quantum Paraelectric State in Kitaev Spin Liquid Candidate $\text{H}_3\text{LiIr}_2\text{O}_6$ Shuai Wang,¹ Long Zhang,^{2,3,*} and Fa Wang^{1,4,†}¹International Center for Quantum Materials, School of Physics, Peking University, Beijing 100871, China²Kavli Institute for Theoretical Sciences and CAS Center for Excellence in Topological Quantum Computation, University of Chinese Academy of Sciences, Beijing 100190, China³Physical Science Laboratory, Huairou National Comprehensive Science Center, Beijing 101400, China⁴Collaborative Innovation Center of Quantum Matter, Beijing 100871, China

(Dated: February 25, 2022)

A new quantum spin liquid (QSL) candidate material $\text{H}_3\text{LiIr}_2\text{O}_6$ was synthesized recently and was found not to show any magnetic order or phase transition down to low temperatures. In this work, we study the quantum dynamics of the hydrogen ions, i.e., protons, in this material by combining first-principles calculations and theoretical analysis. We show that each proton and its adjacent oxygen ions form an electric dipole. The dipole interactions and the proton tunneling are captured by a transverse-field Ising model with a quantum disordered paraelectric ground state. The dipole excitations have an energy gap $\Delta_d \simeq 60$ meV, and can be probed by the infrared optical spectroscopy and the dielectric response. We argue that the electric dipole fluctuations renormalize the magnetic interactions in $\text{H}_3\text{LiIr}_2\text{O}_6$ and lead to a Kitaev QSL state.

PACS numbers: 75.10.Jm, 77.22.-d, 77.84.Bw

I. INTRODUCTION

Quantum spin liquids (QSLs) are paramagnetic ground states of Mott insulators without any long-range magnetic orders or lattice symmetry breaking, which can be induced by (geometrical) frustration¹ and strong charge fluctuations². The QSLs are characterized by fractionalized spinons and emergent gauge flux excitations^{3,4}. They were proposed to be the parent states of high- T_c superconductors^{5,6} and may be used for quantum computation^{7,8}.

The Kitaev model on the honeycomb lattice⁸ is a prototype of QSL. The Hamiltonian hosts the bond-dependent Ising-type interactions,

$$H_K = K \sum_{\langle ij \rangle \in \gamma} S_i^\gamma S_j^\gamma, \quad (1)$$

where $\gamma = x, y, z$ labels the three types of nearest-neighbor bonds [Fig. 1, (b)]. The Kitaev model is exactly solvable with a QSL ground state⁸. Its excitations can be represented by Majorana fermions and emergent \mathbb{Z}_2 gauge fluxes.

It was soon realized⁹ that the Kitaev interaction naturally arises in several transition metal compounds, e.g., Na_2IrO_3 , $\alpha\text{-Li}_2\text{IrO}_3$, and $\alpha\text{-RuCl}_3$ ¹⁰. In these quasi-two dimensional materials, the edge-sharing IrO_6 (RuCl_6) octahedra form a honeycomb lattice in the ab plane. The strong spin-orbit coupling on the cations lifts the degeneracy of the t_{2g} orbitals and leaves a pseudospin $J_{\text{eff}} = 1/2$ Kramers pair occupied by one electron. The anion-mediated electron hopping projected in this subband is strongly suppressed due to the destructive interference of the two Ir-O-Ir hopping paths⁹. The leading-order magnetic interaction involves the Hund coupling on the cations and has exactly the form of the Kitaev term⁹.

However, all these Kitaev QSL candidates turn out to have long-range magnetic orders at low

temperatures^{11–16}. This can be accounted for by the nonnegligible Heisenberg interactions up to third nearest neighbors¹⁷,

$$H_J = J_1 \sum_{\langle ij \rangle} \vec{S}_i \cdot \vec{S}_j + J_2 \sum_{\langle\langle ij \rangle\rangle} \vec{S}_i \cdot \vec{S}_j + J_3 \sum_{\langle\langle\langle ij \rangle\rangle\rangle} \vec{S}_i \cdot \vec{S}_j, \quad (2)$$

and/or other spin-anisotropic interactions¹⁸.

A new Kitaev candidate material, $\text{H}_3\text{LiIr}_2\text{O}_6$, was synthesized recently by substituting hydrogen for the inter- IrO_3 -layer lithium ions in $\alpha\text{-Li}_2\text{IrO}_3$ ¹⁹. The nuclear magnetic resonance and thermodynamic measurements did not find any magnetic order or spin glassiness down to 50 mK despite a large Curie-Weiss temperature $\theta_{\text{CW}} = -105$ K, thus suggesting a QSL state.

In this work, we study $\text{H}_3\text{LiIr}_2\text{O}_6$ with first-principles calculations and theoretical analysis, focusing on the role of the substitute hydrogen ions. We find that each hydrogen ion, i.e., proton, together with two adjacent oxygen ions, forms a uniaxial electric dipole almost perpendicular to the ab plane. The electric dipole-dipole interaction is described by the Ising model on the ABC-stacking triangular lattice. The quantum tunneling of the proton flips the electric dipole and corresponds to a strong transverse field term in the Ising model, and leads to a quantum disordered paraelectric ground state. We thus predict a sizable dielectric response in a broad temperature range. The dipole excitations correspond to an optical phonon mode and can be probed by the infrared optical spectroscopy. We argue that the electric dipole fluctuations can renormalize the magnetic interaction parameters and may push the effective Kitaev-Heisenberg model of $\text{H}_3\text{LiIr}_2\text{O}_6$ into the Kitaev QSL phase.

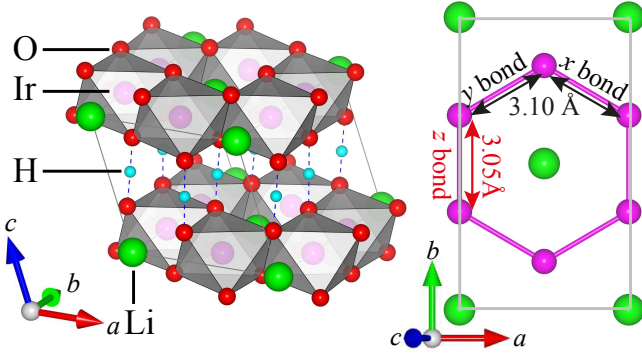


FIG. 1. (a) Crystal structure of $\text{H}_3\text{LiIr}_2\text{O}_6$ relaxed in first-principles calculations with the C2/m space group, i.e., the hydrogen atoms are restricted in the reflection plane by the space group. (b) The honeycomb lattice of iridium ions in the ab plane. The three types of nearest-neighbor bonds in the Kitaev term are labeled.

II. CRYSTAL STRUCTURE AND ELECTRIC DIPOLES ON THE O-H-O BONDS

Given the sensitivity of the magnetic properties of $\text{H}_3\text{LiIr}_2\text{O}_6$ to the hydrogen substitution, we first study the crystal structure with first-principles calculations and pay particular attention to the impact of the substitute hydrogen ions.

The first-principles calculations are performed with the projector augmented wave (PAW) method^{20,21} and the generalized gradient approximation (GGA) to the exchange-correlation functional²², which are implemented in the Vienna *ab initio* Simulation Package (VASP)^{23,24}. The spin-orbit coupling and the onsite Coulomb interaction on the iridium atoms are included in the noncollinear magnetic calculations. The details of the implementation of first-principles calculations are presented in the Supplemental Materials.

We first adopt the experimental crystal structure of $\text{H}_3\text{LiIr}_2\text{O}_6$ without stacking faults refined with a monoclinic structure and the C2/m space group²⁵. The precise positions of the protons were not determined by the X-ray diffraction, therefore, their positions are fully relaxed and optimized in first-principles calculations until the force on each atom is smaller than $0.01 \text{ eV}/\text{\AA}$.

The relaxed crystal structure that preserves the C2/m symmetry is shown in Fig. 1. The hydrogen ions deviate from the original lithium positions in $\alpha\text{-Li}_2\text{IrO}_3$ and bridge the two nearest oxygen ions in the two adjacent IrO_3 layers, and form an ABC-stacking triangular lattice. The O-H-O bonds are almost perpendicular to the ab plane.

The total energy is further lowered if the proton is shifted away from the O-H-O bond center towards either one of the oxygen ions, which breaks the C2/m symmetry, while its displacement in the ab plane increases the energy significantly. By varying the height of one proton while fixing other protons at the O-H-O bond centers

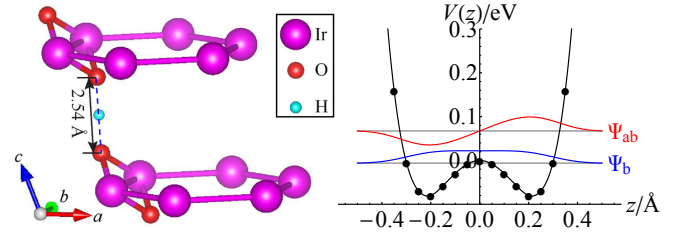


FIG. 2. (a) Schematic illustration of the O-H-O bond, which is almost perpendicular to the ab plane. (b) The 1D double-well potential $V(z)$ along the O-H-O bond direction obtained by interpolating the first-principles energies with one proton placed at different heights (solid circles), where the origin is chosen at the bond center. The proton wavefunctions of the bonding (Ψ_b) and the antibonding (Ψ_{ab}) states are also shown.

in a supercell in the first-principles calculations, we find that the proton is trapped in a double-well potential $V(z)$ [Fig. 2, (b)]. The potential minima are at $\pm 0.22 \text{ \AA}$ away from the O-H-O bond center. We note that there are two types of O-H-O bonds formed by $\text{O}(2)\text{-H}(1)\text{-O}(2)$ and $\text{O}(1)\text{-H}(2)\text{-O}(1)$ with the bond lengths 2.54 \AA and 2.46 \AA , respectively. The proton energy potentials and the electric dipole moments of them are different. The results presented in 2 correspond to the $\text{O}(2)\text{-H}(1)\text{-O}(2)$ bonds. The results of the $\text{O}(1)\text{-H}(2)\text{-O}(1)$ bonds are presented in the Supplemental Materials.

The proton at one of the energy minima forms a uniaxial electric dipole with the oxygen ions. The net dipole moment is calculated by integrating the dipole moment density over a cylinder surrounding the O-H-O bond, $p_0 = 0.06 \sim 0.11 \text{ e} \cdot \text{\AA}$. (The uncertainty comes from different choices of the cylinder height.)

III. ELECTRIC DIPOLE-DIPOLE INTERACTIONS

We treat these uniaxial electric dipoles as Ising variables, $\sigma_i^z = \pm 1$. In order to capture the dipole-dipole interactions in the crystal, we obtain the total energies of various dipole configurations from the first-principles calculations (Fig. 3) and fit the Ising model on the ABC-stacking triangular lattice,

$$H_D = \sum_{ij} D_{ij} \sigma_i^z \sigma_j^z, \quad (3)$$

where D_{ij} denotes both the intralayer interactions $D_{1,2,3}$ and the interlayer interactions $D'_{1,2,3}$ up to the third nearest neighbors defined in Fig. 3. This method was adopted to study the electric dipole-dipole interactions in the hexaferrite $\text{BaFe}_{12}\text{O}_{19}$ ²⁶. The least-square fitting yields $D_1 = 1.7 \text{ meV}$, $D_2 = -0.5 \text{ meV}$, $D_3 = -0.3 \text{ meV}$, $D'_1 = -0.2 \text{ meV}$, $D'_2 = 1.0 \text{ meV}$, and $D'_3 = 0.1 \text{ meV}$. The details are presented in the Supplemental Materials. The

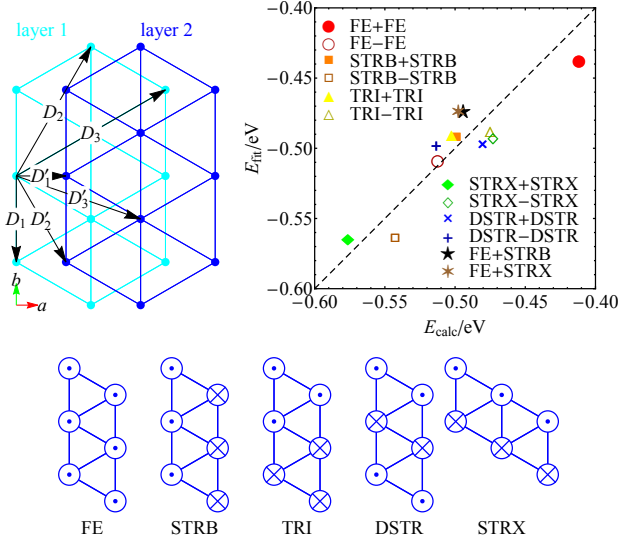


FIG. 3. (a) ABC-stacking triangular lattice of the electric dipoles. The Ising interaction parameters $D_{1,2,3}$ (intralayer) and $D'_{1,2,3}$ (interlayer) are labeled on the corresponding bonds. (b) The comparison of the total energies from first-principles calculations E_{calc} (horizontal axis) and the interaction energies in the Ising model E_{fit} (vertical axis). The Ising interaction parameters are obtained by the least-square fitting. (c) Several intralayer dipole configurations used in calculations. The label “FE+FE” (“FE−FE”) indicates that one of the two layers has the same dipole configuration (has all dipole directions reversed) as the other layer. The dots and the crosses in the schematic dipole configurations stand for the electric dipoles pointing upward or downward, respectively.

comparison of the first-principles total energies and the fitted model energies is shown in Fig. 3. On the other hand, the intralayer nearest-neighbor interaction can be estimated from the dipole-dipole interaction at a distance $r = 3.15 \text{ \AA}$, $D_1 \simeq p_0^2/4\pi\epsilon_0 r^3 = 1.7 \sim 5.6 \text{ meV}$, which is roughly consistent with the result of fitting.

IV. PROTON TUNNELING AND QUANTUM PARAELECTRICITY

The Ising model of the dipole-dipole interactions may suggest an antiferroelectric order at the ground state; however, we will show this is not the case because of the quantum tunneling of the protons. The proton tunneling between the energy minima flips the electric dipole, and thus acts as a transverse field in the Ising model,

$$H_h = -h_x \sum_i \sigma_i^x. \quad (4)$$

h_x can be calculated from the difference of the bonding and the antibonding state energies, ϵ_b and ϵ_{ab} , in the double-well potential $V(z)$. By numerically solving the

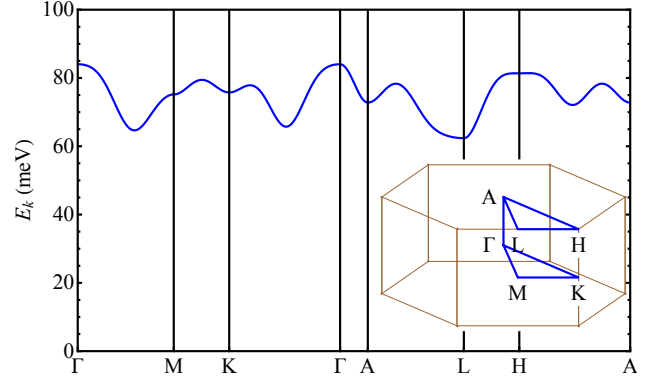


FIG. 4. The dipole excitation spectrum along the high-symmetry lines in the momentum space (inset).

1D Schrödinger equation,

$$-\frac{\hbar^2}{2m_p} \psi''(z) + V(z)\psi(z) = \epsilon\psi(z), \quad (5)$$

where m_p is the proton mass, we find $h_x = (\epsilon_{ab} - \epsilon_b)/2 = 36.7 \text{ meV}$. The wavefunctions of the bonding and the antibonding states are shown in Fig. 2.

The proton tunneling term dominates over the dipole interactions, $h_x \gg |D_{ij}|$, therefore the ground state of the electric dipoles is a quantum disordered paraelectric state and the C2/m symmetry is thus dynamically restored. This leads to the following predictions to experiments. First, these electric dipoles contribute a sizable uniaxial dielectric response to the electric field perpendicular to the ab plane in a large temperature range. The temperature-dependence of the electric susceptibility $\chi_e(T)$ can be derived by the mean field theory of the transverse-field Ising model, and the result is the Barrett formula²⁷,

$$\chi_e(T) = \frac{M}{\frac{1}{2}T_1 \coth(T_1/2T) - T_0}, \quad (6)$$

where $T_1 = 2h_x/k_B \simeq 870 \text{ K}$ marks the crossover from the high- T Curie-Weiss behavior to the low- T plateau, $\chi_e(T \rightarrow 0) = M/(T_1/2 - T_0)$, and $T_0 = -k_B^{-1} \sum_j D_{ij} \simeq -130 \text{ K}$ is the effective antiferroelectric interaction strength. The overall amplitude $M = \rho_0 p_0^2/\epsilon_0 k_B$ depends on the electric dipole moment p_0 and the dipole density ρ_0 .

Second, the electric dipole excitations correspond to an optical phonon mode. Its spectrum is derived by a single-mode approximation on the paraelectric ground state and is shown in Fig. 4. There is a dipole excitation gap $\Delta_d \simeq 60 \text{ meV}$. These dipole excitations may be probed by the infrared optical spectroscopy.

V. DISCUSSION: IMPACT ON THE MAGNETIC INTERACTIONS

The magnetic interactions can be extracted from the total energies of various magnetic moment configurations when both the atom positions and the magnetic moment configurations are prescribed in the first-principles calculations. The details are presented in the Supplemental Materials. The protons are placed at the O-H-O bond centers preserving the C2/m symmetry. The following (extended) Kitaev-Heisenberg model is fitted to the calculated total energies of various magnetic configurations,

$$H_{\text{KH}} = H_K + H_J + \Gamma \sum_{\langle ij \rangle \in \gamma} (S_i^\alpha S_j^\beta + S_i^\beta S_j^\alpha) + \Gamma' \sum_{\langle ij \rangle \in \gamma} (S_i^\alpha S_j^\gamma + S_i^\gamma S_j^\alpha + S_i^\beta S_j^\gamma + S_i^\gamma S_j^\beta), \quad (7)$$

where (α, β, γ) is the cyclic permutation of (x, y, z) . The fitted parameters are listed in Table I. The Curie-Weiss temperature of this model is $\theta_{\text{CW}} = -K - 3J_1 - 6J_2 - 3J_3 = -104$ K. The results of the closely related materials Na_2IrO_3 and $\alpha\text{-Li}_2\text{IrO}_3$ derived from first-principles calculations²⁸ and nonperturbative exact diagonalization²⁹ are also listed in Table I for comparison.

It is instructive to compare the magnetic interaction parameters of $\text{H}_3\text{LiIr}_2\text{O}_6$ and Na_2IrO_3 . In both materials, the spin-anisotropic Γ and Γ' terms as well as the J_2 term are relatively small, which suggests a minimal model incorporating only the K - J_1 - J_3 terms²⁹, which is not applicable to $\alpha\text{-Li}_2\text{IrO}_3$ due to a large Γ term. The phase diagram of this model is obtained by exact diagonalization on small lattice clusters (Fig. 5)²⁹. Both J_1 and J_3 terms can destabilize the Kitaev QSL phase and lead to magnetic ordered states. In particular, a sizable J_3 term favors the zigzag order, which is consistent with the experiments on Na_2IrO_3 ^{11–13}. Both ratios $J_1/|K|$ and $J_3/|K|$ in $\text{H}_3\text{LiIr}_2\text{O}_6$ are significantly reduced upon the hydrogen substitution, thus its ground state is closer to the Kitaev QSL phase. Nevertheless, the fitted K - J_1 - J_3 model of $\text{H}_3\text{LiIr}_2\text{O}_6$ remains in the zigzag ordered phase.

We argue that the proton fluctuations may further

TABLE I. The magnetic interaction parameters (in meV) of $\text{H}_3\text{LiIr}_2\text{O}_6$ derived from first-principles calculations with the hydrogen ions placed at the O-H-O bond centers. The results of Na_2IrO_3 and $\alpha\text{-Li}_2\text{IrO}_3$ reported in Refs.²⁸ and²⁹ are included for comparison. The parameters cited from Ref.²⁹ are averaged over the three bond directions.

Material	K	J_1	J_2	J_3	Γ	Γ'
$\text{H}_3\text{LiIr}_2\text{O}_6$	-21.6	6.3	0.4	3.1	-0.2	-4.1
Na_2IrO_3 ²⁸	-19.1	7.2	-1.6	7.8	1.5	-3.5
Na_2IrO_3 ²⁹	-16.8	0.5	0.2	6.7	1.4	-2.1
$\alpha\text{-Li}_2\text{IrO}_3$ ²⁹	-8.6	-2.7	0.4	6.0	8.9	-0.6

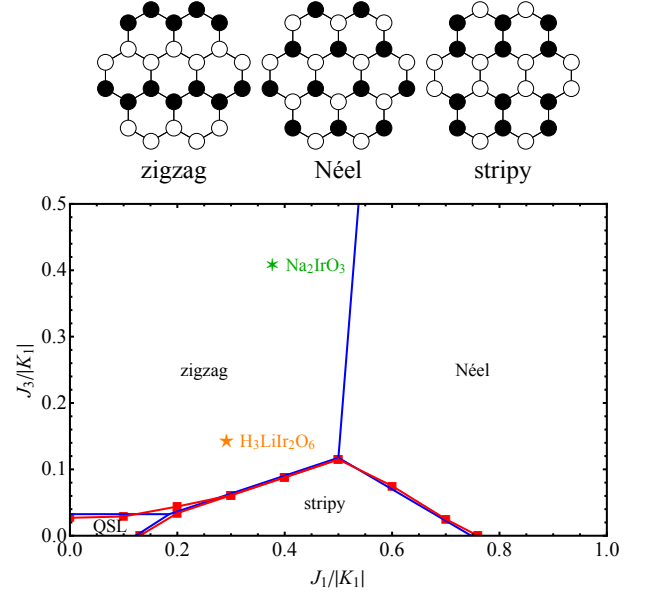


FIG. 5. Phase diagram of the K - J_1 - J_3 model obtained by exact diagonalization on a 24-site cluster (blue lines) and on a 32-site cluster (red lines). The parameters of Na_2IrO_3 and $\text{H}_3\text{LiIr}_2\text{O}_6$ are labeled.

push the effective magnetic interaction parameters of $\text{H}_3\text{LiIr}_2\text{O}_6$ into the Kitaev QSL phase. Recall that the oxygen-mediated nearest-neighbor electron hopping in the Slater-Koster approximation exactly vanishes in the pseudospin $J_{\text{eff}} = 1/2$ subspace due to the destructive interference of the two Ir-O-Ir hopping paths⁹. This exact cancellation is absent when the fluctuations of the nearby protons set in and the two hopping paths are not equivalent. When the proton gets closer to one of the oxygen ions, the onsite energy of a hole at this oxygen ion is increased, $E_p \rightarrow E_p + \delta E_p$, thus the hopping amplitude along this path is reduced, $t \rightarrow t - \delta t$, with $\delta t/t \simeq \delta E_p/E_p$, and the two hopping paths do not cancel out completely. For example, on a z -bond, the remnant hopping term is

$$\delta H_t = -\frac{1}{3}\delta t(\sigma_1^z + \sigma_2^z) \sum_{\alpha} i\alpha d_{j\alpha}^\dagger d_{i\alpha} + \text{h.c.}, \quad (8)$$

where $d_{j\alpha}^\dagger$ is the creation operator of the pseudospin $J_{\text{eff}} = 1/2$ electron on the iridium ion, and σ_1^z and σ_2^z are the configurations of the two dipoles close to the two oxygen ions, respectively. Treating it as a perturbation gives the following correction to the effective magnetic interactions,

$$\delta H_{\text{KH}} = \delta J \sum_{\langle ij \rangle \in \gamma} (2S_i^\gamma S_j^\gamma - \vec{S}_i \cdot \vec{S}_j), \quad (9)$$

where $\delta J = 8\delta t^2/9(U + 2h_x)$ and U is the onsite repulsion on the iridium ions. Therefore, the proton fluctuations renormalize the magnetic interaction parameters,

$|K| \rightarrow |K| - 2\delta J$, and $J_1 \rightarrow J_1 - \delta J$. The ratio $J_1/|K|$ is nevertheless reduced because $J_1/|K| < 0.5$. By considering the oxygen-mediated long-range hopping paths, we may similarly argue that J_3 is also reduced by the proton fluctuations. Therefore, the proton/electric dipole fluctuations may further push the magnetic interactions towards the Kitaev QSL phase.

VI. SUMMARY AND OUTLOOK

We have studied the physical consequences of the hydrogen substitution in the Kitaev QSL candidate $\text{H}_3\text{LiIr}_2\text{O}_6$. We find that each proton is trapped in a double-well potential and forms an electric dipole with two adjacent oxygen ions. Incorporating the dipole interactions and the proton tunneling, the low-energy dynamics of these dipoles is captured by a transverse-field Ising model. The strong proton tunneling leads to a quantum disordered paraelectric ground state. The dipole excitations may be probed with the dielectric response and the infrared optical spectroscopy. The dipole fluctuations renormalize the effective magnetic interactions and may push the magnetic ground state of $\text{H}_3\text{LiIr}_2\text{O}_6$ into the Kitaev QSL phase. Similar study of the role of the hydrogen ions in $\text{H}_3\text{LiIr}_2\text{O}_6$ was also presented in two independent works published recently^{30,31}. Evidence of the proposed quantum paraelectricity has been obtained in recent experiments with dielectric spectroscopy³².

The electric dipoles formed by displaced ions are ubiquitous in materials. Our approach to the quantum dynamics of the electric dipoles can be applied to other

materials. Moreover, the interplay of the electric dipoles and the spin and orbit degrees of freedom may provide a new route towards quantum paraelectric states, QSLs and other exotic quantum states of matter^{33–36}.

In this work, we have not analyzed the unusual thermodynamic behaviors of $\text{H}_3\text{LiIr}_2\text{O}_6$ found in the experiments¹⁹. In a recent theoretical work accounting for this behavior³⁷ was based on the assumption that a single layer of $\text{H}_3\text{LiIr}_2\text{O}_6$ would be in the Kitaev QSL phase. On the other hand, it was also proposed that the low-energy excitations could be attributed to a random singlet phase³⁸, which is qualitative consistent with the recent experimental evidence of slowing-down dynamics in the dielectric response at low temperature³². The effect of quenched disorder on the thermodynamic and magnetic properties in $\text{H}_3\text{LiIr}_2\text{O}_6$ and other related materials is worth further study.

ACKNOWLEDGMENTS

We are grateful to inspiring discussions with Xingye Lu and Weiqiang Yu. The numerical simulations were performed on Tianhe-I Supercomputer System in Tianjin and on Tianhe-II Supercomputer System in Guangzhou. This work is supported by National Key Basic Research Program of China (No. 2014CB920902), National Key R&D Program of China (Nos. 2017YFA0302904 and 2018YFA0305800), National Natural Science Foundation of China (No. 11804337), Strategic Priority Research Program of Chinese Academy of Sciences (No. XDB28000000), and Beijing Municipal Science & Technology Commission (No. Z181100004218001).

* longzhang@ucas.ac.cn

† wangfa@pku.edu.cn

¹ L. Balents, *Nature* **464**, 199 (2010).

² Y. Zhou, K. Kanoda, and T.-K. Ng, *Rev. Mod. Phys.* **89**, 025003 (2017).

³ X.-G. Wen, *Quantum field theory of many-body systems: from the origin of sound to an origin of light and electrons* (Oxford University Press, 2004).

⁴ X.-G. Wen, *Phys. Rev. B* **65**, 165113 (2002).

⁵ P. W. Anderson, *Science* **235**, 1196 (1987).

⁶ P. A. Lee, N. Nagaosa, and X.-G. Wen, *Rev. Mod. Phys.* **78**, 17 (2006).

⁷ A. Kitaev, *Ann. Phys. (N. Y.)* **303**, 2 (2003).

⁸ A. Kitaev, *Ann. Phys. (N. Y.)* **321**, 2 (2006).

⁹ G. Jackeli and G. Khaliullin, *Phys. Rev. Lett.* **102**, 017205 (2009).

¹⁰ K. W. Plumb, J. P. Clancy, L. J. Sandilands, V. V. Shankar, Y. F. Hu, K. S. Burch, H.-Y. Kee, and Y.-J. Kim, *Phys. Rev. B* **90**, 041112 (2014).

¹¹ X. Liu, T. Berlijn, W.-G. Yin, W. Ku, A. Tsvelik, Y.-J. Kim, H. Gretarsson, Y. Singh, P. Gegenwart, and J. P. Hill, *Phys. Rev. B* **83**, 220403 (2011).

¹² S. K. Choi, R. Coldea, A. N. Kolmogorov, T. Lancaster, I. I. Mazin, S. J. Blundell, P. G. Radaelli, Y. Singh, P. Gegenwart, K. R. Choi, S.-W. Cheong, P. J. Baker, C. Stock, and J. Taylor, *Phys. Rev. Lett.* **108**, 127204 (2012).

¹³ F. Ye, S. Chi, H. Cao, B. C. Chakoumakos, J. A. Fernandez-Baca, R. Custelcean, T. F. Qi, O. B. Korneta, and G. Cao, *Phys. Rev. B* **85**, 180403 (2012).

¹⁴ J. A. Sears, M. Songvilay, K. W. Plumb, J. P. Clancy, Y. Qiu, Y. Zhao, D. Parshall, and Y.-J. Kim, *Phys. Rev. B* **91**, 144420 (2015).

¹⁵ R. D. Johnson, S. C. Williams, A. A. Haghighirad, J. Singleton, V. Zapf, P. Manuel, I. I. Mazin, Y. Li, H. O. Jeschke, R. Valentí, and R. Coldea, *Phys. Rev. B* **92**, 235119 (2015).

¹⁶ S. C. Williams, R. D. Johnson, F. Freund, S. Choi, A. Jesche, I. Kimchi, S. Manni, A. Bombardi, P. Manuel, P. Gegenwart, and R. Coldea, *Phys. Rev. B* **93**, 195158 (2016).

¹⁷ I. Kimchi and Y.-Z. You, *Phys. Rev. B* **84**, 180407 (2011).

¹⁸ J. G. Rau, E. K.-H. Lee, and H.-Y. Kee, *Phys. Rev. Lett.* **112**, 077204 (2014).

- ¹⁹ K. Kitagawa, T. Takayama, Y. Matsumoto, A. Kato, R. Takano, Y. Kishimoto, S. Bette, R. Dinnebier, G. Jackeli, and H. Takagi, *Nature* **554**, 341 (2018).
- ²⁰ P. E. Blöchl, *Phys. Rev. B* **50**, 17953 (1994).
- ²¹ G. Kresse and D. Joubert, *Phys. Rev. B* **59**, 1758 (1999).
- ²² J. P. Perdew, K. Burke, and M. Ernzerhof, *Phys. Rev. Lett.* **77**, 3865 (1996).
- ²³ G. Kresse and J. Furthmüller, *Comput. Mater. Sci.* **6**, 15 (1996).
- ²⁴ G. Kresse and J. Furthmüller, *Phys. Rev. B* **54**, 11169 (1996).
- ²⁵ S. Bette, T. Takayama, K. Kitagawa, R. Takano, H. Takagi, and R. E. Dinnebier, *Dalt. Trans.* **46**, 15216 (2017).
- ²⁶ P. S. Wang and H. J. Xiang, *Phys. Rev. X* **4**, 011035 (2014).
- ²⁷ J. H. Barrett, *Phys. Rev.* **86**, 118 (1952).
- ²⁸ K. Hu, F. Wang, and J. Feng, *Phys. Rev. Lett.* **115**, 167204 (2015).
- ²⁹ S. M. Winter, Y. Li, H. O. Jeschke, and R. Valentí, *Phys. Rev. B* **93**, 214431 (2016).
- ³⁰ Y. Li, S. M. Winter, and R. Valentí, *Phys. Rev. Lett.* **121**, 247202 (2018).
- ³¹ R. Yadav, R. Ray, M. S. Eldeeb, S. Nishimoto, L. Hozoi, and J. van den Brink, *Phys. Rev. Lett.* **121**, 197203 (2018).
- ³² K. Geirhos, P. Lunkenheimer, M. Blankenhorn, R. Claus, Y. Matsumoto, K. Kitagawa, T. Takayama, H. Takagi, I. Kézsmárki, and A. Loidl, arXiv:2002.09016.
- ³³ S.-P. Shen, J.-C. Wu, J.-D. Song, X.-F. Sun, Y.-F. Yang, Y.-S. Chai, D.-S. Shang, S.-G. Wang, J. F. Scott, and Y. Sun, *Nat. Commun.* **7**, 10569 (2016).
- ³⁴ M. Shimozawa, K. Hashimoto, A. Ueda, Y. Suzuki, K. Sugii, S. Yamada, Y. Imai, R. Kobayashi, K. Itoh, S. Iguchi, M. Naka, S. Ishihara, H. Mori, T. Sasaki, and M. Yamashita, *Nat. Commun.* **8**, 1821 (2017).
- ³⁵ N. Hassan, S. Cunningham, M. Mourigal, E. I. Zhilyaeva, S. A. Torunova, R. N. Lyubovskaya, J. A. Schlueter, and N. Drichko, *Science* **360**, 1101 (2018).
- ³⁶ J. Zheng, Y. Cui, T. Li, K. Ran, J. Wen, and W. Yu, *Sci. China Physics, Mech. Astron.* **61**, 057021 (2018).
- ³⁷ K. Slagle, W. Choi, L. E. Chern, and Y. B. Kim, *Phys. Rev. B* **97**, 115159 (2018).
- ³⁸ I. Kimchi, J. P. Sheckelton, T. M. McQueen, and P. A. Lee, *Nat. Commun.* **9**, 4367 (2018).